Resistive tearing mode instability with shear flow and viscosity

L. Ofman, X. L. Chen, and P. J. Morrison
Department of Physics and Institute for Fusion Studies, The University of Texas at Austin, Austin, Texas 78712

R. S. Steinolfson
Department of Space Sciences, Southwest Research Institute, San Antonio, Texas 78228

(Received 27 August 1990; accepted 18 February 1991)

The linear theory of the resistive tearing mode instability in slab geometry, has been recently extended by introducing the effect of equilibrium shear flow and viscosity [Phys. Fluids **29**, 2563 (1986); Phys. Fluids B **1**, 2224 (1989); *ibid.* **2**, 495 (1990); *ibid.* **2**, 2575 (1990)]. In the present analysis, numerical solutions of the time-dependent resistive equations are generalized to this problem and growth rate scaling is obtained. The results of the computations are compared to previous work, and the computed growth rate scalings agree with analytical predictions. Namely, the "constant-ψ" growth rate scales as $S^{-1/2}$ and the "nonconstant-ψ" growth rate scales as $S^{-1/3}$, where S is the magnetic Reynolds number. The Furth–Killeen–Rosenbluth (FKR) scaling of $S^{-3/5}$ is reproduced for small values of shear flow. The presence of flow introduces a new peak in the eigenfunction, which is outside of the peak that occurs in the case without flow. The introduction of viscosity and small shear alters the growth rate scaling to $S^{-2/3}(S_v/S)^{1/6}$ where S_v is the ratio of the viscous time to the Alfvén time. When the shear flow is large, the growth rate behaves in a more complex way, and Kelvin–Helmholtz instability effects are present.

I. INTRODUCTION

Magnetic reconnection was first suggested by Dungey[1] to explain energy release in solar flares and other astrophysical phenomena, and since then the topic has been studied extensively. Furth, Killeen, and Rosenbluth[2] (hereafter FKR) developed an analytic boundary-layer theory of resistive magnetic tearing, and numerical techniques have subsequently been applied to the problem.[3]

FKR theory has been widely used and applied to laboratory plasmas and fusion experiments in various geometries. Numerical computations of linear tearing mode instability have been performed by many, in various subvolumes of parameter space (see, for example, Steinolfson and Van Hoven[4]), usually without equilibrium shear flow or viscosity effects. The importance of flow and viscosity in the evolution of tearing instability growth rate scaling has been recently shown using both analytical[5–9] and numerical[10–12] analyses. Nonhomogeneous flows are commonly observed in various phenomena believed to involve reconnection, such as solar coronal loops, magnetopause boundary, solar wind, extragalactic jets, and fusion experiments.[13,14]

We solve the time-dependent equations numerically throughout the entire physical region of instability, in contrast to the boundary-layer approach in which solutions of two physically different regions must be matched. This approach enables us to avoid some significant assumptions required by the boundary-layer theory, such as "constant-ψ" or conditions on the growth rate γ (Refs. 5 and 6) (see Sec. III). Thus, we can test the validity of these assumptions and corroborate various scaling laws predicted analytically.

Using a finite difference method for the time-dependent problem, we are able to show the spatial and temporal evolution of the perturbed quantities and the dependence on the physical parameters of the problem. Some relevant parameters examined in our study are the normalized wave number α, the magnetic Reynolds number S, the shear parameter R, the fluid velocity V (normalized to Alfvén velocity), and the ratio between viscous and Alfvén time scales S_v.

In Refs. 10 and 11 the authors solve Eqs. (9) and (10) using a different approach. A system of algebraic equations resulting from the finite difference equations is solved as an eigenvalue problem. In order to obtain a nontrivial solution the determinant of the coefficients of the system must vanish. The value of the growth rate γ that makes the determinant vanish is the eigenfrequency of the mode. The difficulty of this method, as stated by the authors, is the need to search for zeros in the complex plane and identifying the eigenfrequency being sought. In the time-dependent approach of the present paper, the correct growth rate emerges "naturally" from the solution of the initial value problem. The numerical value of γ is obtained rather easily with a well-known fast Fourier transform (FFT) technique. By retaining the time dependence, we are able to study cases on a relatively short time scale, such as may be necessary when more than one overstable mode is present in the solutions. This is particularly significant for the nonlinear simulations in which several modes can interact.[15]

The paper is organized as follows. In Sec. II we present the basic equations. In Sec. III the main results of the linear boundary-layer theory are reviewed. In Sec. IV the method of solution is described. Section V is devoted to the results of numerical computations. Summary and discussion are presented in Sec. VI.

 0899-8221/91/061364-10$02.00

II. BASIC EQUATIONS

We assume that collisional magnetohydrodynamic (MHD) theory[16] is applicable, that the plasma is incompressible with constant isotropic resistivity η and constant perpendicular viscosity[5,17] ν, and that gravitational effects are negligible. The basic equations in cgs units are

$$\rho\left(\frac{\partial \mathbf{v}}{\partial t}+(\mathbf{v}\cdot\nabla)\mathbf{v}\right)=-\nabla p+\frac{1}{4\pi}(\nabla\times\mathbf{B})\times\mathbf{B}+\nu\nabla_1^2\mathbf{v}, \tag{1}$$

$$\frac{\partial \mathbf{B}}{\partial t}=\nabla\times(\mathbf{v}\times\mathbf{B})-\frac{c^2\eta}{4\pi}\nabla\times(\nabla\times\mathbf{B}), \tag{2}$$

$$\nabla\cdot\mathbf{v}=0, \quad \nabla\cdot\mathbf{B}=0, \tag{3}$$

where c is the speed of light, ρ is the plasma density, $\mathbf{B}$ is the magnetic field, and $\mathbf{v}$ is the velocity of the plasma. The pressure p is eliminated from the calculations by taking a curl of Eq. (1).

We use Cartesian geometry and choose an equilibrium magnetic field of the form

$$\mathbf{B}_0(y)=B_{x0}(y)\mathbf{e}_x+B_{z0}(y)\mathbf{e}_z.$$

Similarly, the equilibrium plasma flow is assumed to be in the (x,z) plane, with the form

$$\mathbf{v}_0(y)=v_{x0}(y)\mathbf{e}_x+v_{z0}(y)\mathbf{e}_z.$$

Equations (1)–(3) are linearized around the magnetic field and flow velocity equilibrium solutions assuming perturbations of the form $f_1(y,t)\exp(ik_x x+ik_z z)$. The normalized linearized time-dependent y components of the MHD equations can be written as

$$\left(\frac{\partial}{\partial\tau}+i\alpha G\right)(W''-\alpha^2 W)-i\alpha R^2 G'' W$$
$$=i\alpha F(\psi''-\alpha^2\psi)-i\alpha F''\psi+\frac{1}{S_v}\frac{\partial^4 W}{\partial\mu^4}, \tag{4}$$

$$\left(\frac{\partial}{\partial\tau}+i\alpha G\right)\psi-i\alpha F W=S^{-1}(\psi''-\alpha^2\psi), \tag{5}$$

where the dimensionless variables are $\tau=t/\tau_H$, $\mu=y/a_b$, and the perturbed physical quantities $\psi=B_{y1}/B$, $W=V_{y1}/V_a$. Also, the dimensionless parameters are the magnetic Reynolds number $S=\tau_r/\tau_H$, a measure of viscosity $S_v=\tau_v/\tau_H$, the shear parameter $R=a_b/a_v$, and the normalized wave number $\alpha=ka_b$.

The relevant time scales in these definitions are the resistive time τ_r, the Alfvén time τ_H, and the viscous time τ_v given by

$$\tau_v=\frac{\rho a_b^2}{\nu}, \quad \tau_r=\frac{4\pi a_b^2}{c^2\eta}, \quad \tau_H=\frac{a_b(4\pi\rho)^{1/2}}{B},$$

and in the above quantities a_b is the magnetic length scale, a_v is the velocity length scale, V_a is the Alfvén velocity, and B is a measure of the magnetic field. The equilibrium magnetic field and flow velocity are given by

$$F=(k_x B_{x0}+k_z B_{z0})/kB,$$
$$G=(k_x V_{x0}+k_z V_{z0})/kV_a.$$

Specifically we choose $k_z=0$ and the following forms of F and G:

$$F=\tanh\mu, \tag{6}$$

$$G=V\tanh(R\mu), \tag{7a}$$

or

$$G=V[\operatorname{sech}(R\mu)-1], \tag{7b}$$

where V is the velocity parameter in units of V_a and R is the shear parameter. Hereafter we refer to Eq. (7a) as the "tanh" velocity profile, where Eq. (7b) will be referred to as the "sech" profile.

Equations (4) and (5) are solved numerically without any further approximations. They are subject to the boundary conditions that W, $\psi\to 0$ exponentially when $\mu\to\pm\infty$. For the numerical simulation limited to finite boundaries located at μ_1 and μ_2, the above boundary conditions become

$$W'(\mu_{1,2})=\pm\alpha W(\mu_{1,2}),$$
$$\psi'(\mu_{1,2})=\pm\alpha\psi(\mu_{1,2}), \tag{8}$$

where primes denote the derivatives with respect to μ taken at the left (μ_1) and right (μ_2) boundaries of the physical region.

III. LINEAR THEORY

The growth rates of the instability can be found from the time-Fourier-transformed equations (4) and (5), using the boundary-layer approach.[2,5–9] Assuming perturbations of the form $f_1(y)\exp(i\omega t+ik_x x)$, these equations become

$$(\gamma+i\alpha G)(W''-\alpha^2 W)-i\alpha R^2 G'' W$$
$$=i\alpha F(\psi''-\alpha^2\psi)-i\alpha F''\psi+\frac{1}{S_v}\frac{\partial^4 W}{\partial\mu^4}, \tag{9}$$

$$(\gamma+i\alpha G)\psi-i\alpha F W=S^{-1}(\psi''-\alpha^2\psi), \tag{10}$$

where $\gamma=\gamma_R+i\gamma_I=i\omega\tau_H$ is the complex growth rate and the subscripts R and I denote real and imaginary parts, respectively.

The physical region is divided in two regions, namely, an inner region in which $|F|\ll 1$ and resistivity cannot be neglected [e.g., near $\mu=0$, for $F(\mu)$ as in (6)], and an outer region in which the resistivity can be neglected in Ohm's law. In the inner singular layer, one can substitute $F'(\mu)=F'(0)$, $F''(\mu)=F''(0)$, $G'(\mu)=G'(0)$, $G''(\mu)=G''(0)$, and $F(\mu)=\mu F'(0)$.

The solutions in the outer and inner regions are matched continuously through a matching parameter

$$\Delta'=(\psi_2'/\psi_2)-(\psi_1'/\psi_1),$$

where the subscripts 1 and 2 denote values at the boundaries of the inner singular layer of width ϵ, respectively. An important result obtained by analytical means in Ref. 5 is that flow in the outer region can drastically change the matching quantity Δ'. In fact, alteration of the external flow profile can effect the transition from constant-ψ to nonconstant-ψ tearing. A numerical estimate of Δ' is discussed in Sec. V.

The FKR result, without shear flow or viscosity, is

$$\gamma_R\sim S^{-3/5}. \tag{11}$$

This scaling can be used as a benchmark for comparison with new numerical results.

The growth rates and their scalings are found by match-

ing the resistive and ideal solutions, under the following limits of the parameters that emerge from the inner layer equations:

$$\text{slow growth } |\gamma/\alpha F'(0)\epsilon| \ll 1, \tag{12a}$$

$$\text{fast growth } |\gamma/\alpha F'(0)\epsilon| \sim 1, \tag{12b}$$

$$\text{small shear } |G'(0)/F'(0)| \ll 1, \tag{12c}$$

$$\text{comparable shear } |G'(0)/F'(0)| \sim 1, \tag{12d}$$

where ϵ is the width of the inner layer [hereafter we drop the zeros in (12a)–(12d)].

The results for the inviscid case, as obtained in Ref. 5, are summarized in Table I. The following is a list of growth rates for both inviscid and viscous tearing modes with flow that were obtained analytically in Refs. 5 and 6 and calculated numerically in the present work.

For the nonconstant-ψ tearing mode and small or comparable shear (12c) and (12d), the growth rate scaling is

$$\gamma_R \sim \alpha^{2/3} S^{-1/3}. \tag{13a}$$

In the case of the constant-ψ tearing mode when the velocity shear is comparable to the magnetic shear, (12d), the growth rate scales as

$$\gamma_R \sim \alpha^{1/2} S^{-1/2}. \tag{13b}$$

When viscosity is present and the condition $|G'/F'| < 1$ is satisfied, (13b) is modified to

$$\gamma_R \sim S^{-2/3} Q^{1/3} \left[4\frac{S}{S_v} + \frac{G'^2}{F'^2}\left(1 - \frac{S}{S_v}\right)^2 \right]^{-1/6}, \tag{13c}$$

where $Q \equiv \alpha F'[1 - (G'^2/F'^2)]$. As $|G'/F'| \to 1$, the growth rate approaches zero as $Q^{1/3}$. When $|G'/F'| > 1$, the tearing mode disappears, and Kelvin–Helmholtz (K–H) instability effects are present. When the shear is very small (12c), the growth rate scaling (11) becomes

$$\gamma_R \sim (\alpha F')^{1/3} S^{-2/3} (S_v/S)^{1/6}. \tag{13d}$$

The dependence of the growth rate on S, S_v, and $|G'/F'|$ in Eqs. (13a)–(13d) has been verified numerically. These results will be presented in Sec. V.

IV. METHOD OF SOLUTION

We solve Eqs. (4) and (5) using an implicit finite difference scheme[3,4] with a variable spatial grid. The following system of equations in the complex plane, generalized to accommodate flow and viscosity, is solved numerically:

TABLE I. Summary of the effects of equilibrium shear flow on the tearing mode. (From Chen and Morrison.[5])

	Constant-ψ tearing mode	Nonconstant-ψ tearing mode
$\left\|\frac{G'(0)}{F'(0)}\right\| \ll 1$	(a) The growth rate and scale length of the resistive region are, respectively, $\gamma \sim \alpha^{2/5}\Delta'^{4/5}S^{-3/5}$, $\epsilon \sim (\alpha S)^{-2/5}\Delta'^{1/5} \ll 1$ (b) The constant-ψ approximation is valid if $\epsilon\|\Delta'\| \ll 1$ (c) Small flow shear $G'(0)$ destabilizes the constant-ψ tearing mode	(a) The growth rate and scale length of the resistive region are, respectively, $\gamma \sim \alpha^{2/3}S^{-1/3}$, $\epsilon \sim (\alpha S)^{-1/3} \ll 1$ (b) In this limit, we have $\epsilon\|\Delta'\| \gg 1$, $1 - G'(0)^2/F'(0)^2 \to 0$ (c) Small flow shear $G'(0)$ stabilizes the nonconstant-ψ tearing mode with sufficiently large Δ'
$\left\|\frac{G'(0)}{F'(0)}\right\| \lesssim 1$	(a) The growth rate and scale length of the resistive region are, respectively, $\gamma \sim (\alpha\|\Delta'\|)^{1/2}S^{-1/2}$, $\epsilon \sim (\alpha S)^{-1/3} \ll 1$ (b) If $G'(0)G''(0) - F'(0)F''(0) \neq 0$, $\Delta' > 0$ instability criterion is removed (c) The constant-ψ approximation is valid if $\|\sqrt{[1 - G'(0)^2/F'(0)^2]\Delta'\epsilon}\| \ll 1$	(d) There exists a transition to ideal instability when Δ' becomes negative through $\Delta' = \infty$ (which is made possible by the flow on the external region)
$\left\|\frac{G'(0)}{F'(0)}\right\| > 1$	stabilized	stabilized

$$-\frac{i\alpha F_j}{2\Delta\mu_j\Delta\mu_+}\psi_{j+1}^{n+1}+i\left(\frac{\alpha F_j}{\Delta\mu_+\Delta\mu_-}+\frac{\alpha^3}{2}F_j+\frac{\alpha F_j''}{2}\right)\psi_j^{n+1}$$
$$-\frac{i\alpha F_j}{2\Delta\mu_j\Delta\mu_-}\psi_{j-1}^{n+1}-\frac{1}{2S_v\Delta\mu_j\Delta\mu_+}Z_{j+1}^{n+1}+\left(\frac{1}{\Delta\tau}+\frac{i\alpha}{2}G_j+\frac{1}{S_v\Delta\mu_-\Delta\mu_+}\right)Z_j^{n+1}$$
$$-\frac{1}{S_v\Delta\mu_j\Delta\mu_-}Z_{j-1}^{n+1}-\left(\frac{\alpha^2}{\Delta\tau}+\frac{i\alpha^3}{2}G_j+\frac{i\alpha}{2}R^2G_j''\right)W_j^{n+1}=k_j^n, \tag{14}$$

$$-\frac{1}{2\Delta\mu_j\Delta\mu_+S}\psi_{j+1}^{n+1}$$
$$+\left(\frac{1}{\Delta\tau}+\frac{i\alpha}{2}G_j+\frac{1}{\Delta\mu_j\Delta\mu_+S}+\frac{\alpha^2}{2S}\right)\psi_j^{n+1}$$
$$-\frac{1}{2\Delta\mu_j\Delta\mu_-S}\psi_{j-1}^{n+1}-\frac{i\alpha}{2}F_jW_j^{n+1}=d_j^n, \tag{15}$$

$$Z_j^{n+1}-\frac{1}{\Delta\mu_j\Delta\mu_+}W_{j+1}^{n+1}+\frac{2}{\Delta\mu_+\Delta\mu_-}W_j^{n+1}$$
$$-\frac{1}{\Delta\mu_j\Delta\mu_-}W_{j-1}^{n+1}=q_j^n, \tag{16}$$

where $\Delta\mu_j=(\mu_{j+1}-\mu_{j-1})/2$, $\Delta\mu_+=\mu_{j+1}-\mu_j$, $\Delta\mu_-=\mu_j-\mu_{j-1}$. The variable grid spacing $\Delta\mu_j$ expands from a minimum of $\Delta\mu_{\min}=10^{-5}$ near the singular surface to $\Delta\mu_{\max}=0.5$ near the computational boundaries according to the prescription

$$\Delta\mu_j=\Delta\mu_{\max}(\Delta\mu_{\min}/\Delta\mu_{\max})^{(J-j)/(J-1)},$$

where J denotes the boundary grid point. Up to 240 grid points were used.

The purpose of Eq. (16), which is a finite difference form of $Z(t,\mu)-W''(t,\mu)=0$, is to enable the numerical calculation of the fourth-order viscous term $S_v^{-1}(\partial^4W/\partial\mu^4)$ in Eq. (4), while maintaining the tridiagonal form of the finite difference equations:

$$-A_jU_{j+1}^{n+1}+B_jU_j^{n+1}-C_jU_{j-1}^{n+1}=P_j^n, \tag{17}$$

where A, B, and C are 3×3 matrices and U and P are three-dimensional vectors. Equation (17) is solved for U by using Gaussian elimination.

The time step $\Delta\tau$ was selected so that $\Delta\tau\leqslant\min(1/\gamma_R,1/5\gamma_I)$, and the simulation was evolved for N time steps until only the fastest growing mode was present in the solutions. Usually the number of time steps satisfied $50<N<500$.

From the complex solutions $W(t,\mu)$ and $\psi(t,\mu)$, which are symmetric or antisymmetric relative to $\mu=0$ [the symmetries are determined by the functions $F(\mu)$ and $G(\mu)$ in Eqs. (4) and (5)], the growth rates were obtained in two steps (see Fig. 1). First, the real part of the growth rate γ_R is found by fitting a straight line to the logarithm of $W(t,\mu_0)$ (where μ_0 is an arbitrary point in the domain). Next, the exponential trend is removed from the solutions and a fast Fourier transform is performed on the remaining oscillatory part of $W(t,\mu_0)$, which thereby determines the imaginary part of the growth rate γ_I. If more than one overstable mode is present at the same time, the result of the FFT will show a corresponding number of well-defined peaks, indicating the values of the γ_I. This occurs when the real parts of the two modes have very close values:

$$\exp(\gamma_{R1}t_m)\exp(-\gamma_{R2}t_m)\sim1, \tag{18}$$

where $t_m=N\Delta\tau$.

If the modes are purely growing (no time-dependent oscillations are present), then only the first step in the above method is performed.

V. NUMERICAL RESULTS

The method of finding the complex growth rate (Sec. IV) is clarified in Fig. 1. In Figs. 2–10 we present the results of computer simulations of tearing mode instability. In Figs. 2–4 the spatial behavior of the complex solutions $W(t_0,\mu)$ and $\psi(t_0,\mu)$, normalized to their respective peak values, is presented. In what follows, we have used the normalizations

$$\psi=B_{y1}/B_{y1\max}\quad\text{and}\quad W=-iV_{y1}/V_{y1\max};$$

the absolute maximal values are given in Table II. Figures 5 and 7–9 show the various scalings of the growth rate, as in Eqs. (13a)–(13d). In Fig. 6, the dependence of the growth rate γ on the shear parameter R, for sech and tanh flow profiles is shown.

In Figs. 2 and 3 the constant-ψ solutions are shown. This is clearly seen from the fact that the tearing layer, defined by the inner peak of W_R, is located in a region where ψ_R is constant. The presence of flow introduces the imaginary parts of the perturbed quantities and the outer peak in W_R, as compared to FKR-type solutions (see, for example, Ref. 4). The inviscid solutions in Figs. 2(a) and 3(a) agree with Ref. 10. The figures of the eigenfunctions in Ref. 10 are drawn with a linear scale in the y direction, rather than the logarithmic scale used in this paper. In Fig. 2(a) the equilibrium magnetic field was (6), the flow profile was tanh (7a), and the velocity shear, determined by $V=1$ and $R=0.73$, was comparable to the magnetic field shear. The antisymmetric solutions, namely, W_R (short-dashed line) and ψ_I (long-dashed line), for the positive and negative values of μ are plotted on the positive logarithmic μ axis. The solutions in Fig. 2(b) are for the same parameters as in Fig. 2(a), but they include viscosity comparable to resistivity $S=S_v=10^6$. Its effect is to reduce W_R and ψ_I relative to ψ_R (see Table II) and therefore, reduce the reconnecting fields and the growth rate. Figs. 3(a) and 3(b) show the behavior for a sech equilibrium flow. In Fig. 3(b) the antisymmetric solutions are W_R and W_I (dashed line). The solid line is ψ_R and in this case it merges with the normalized ψ_I that has similar shape. The effect of viscosity on this solution is

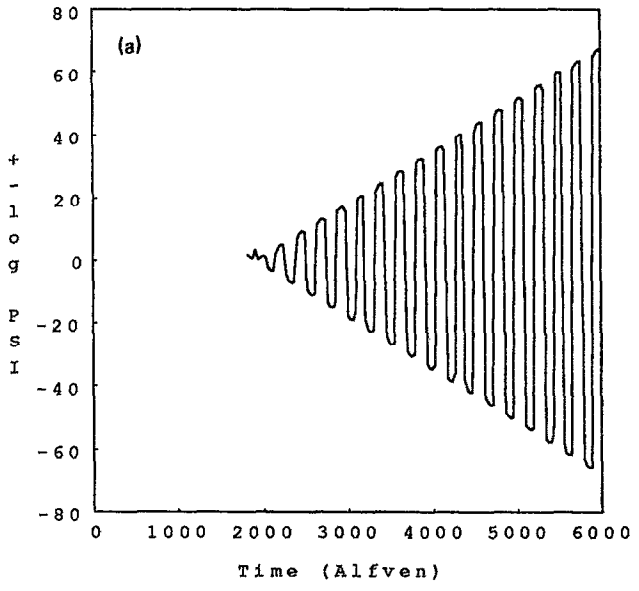

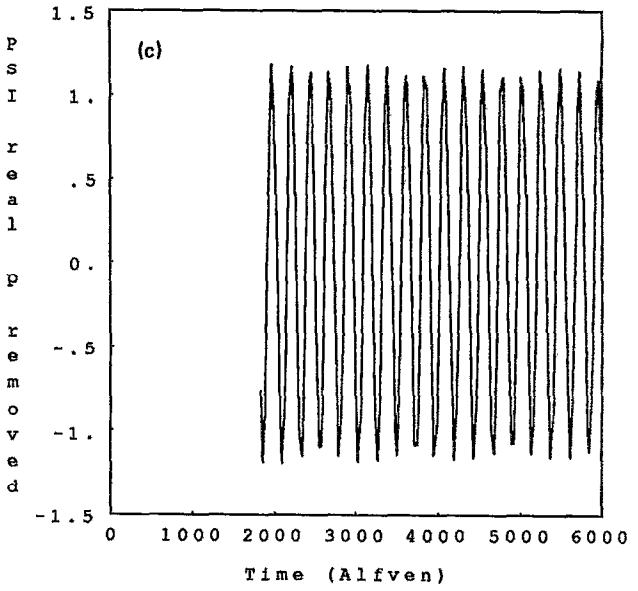

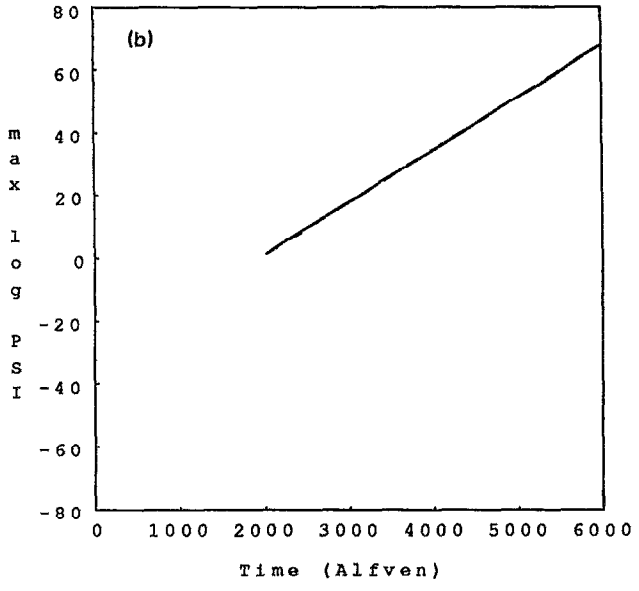

FIG. 1. (a) The time-dependent solution $\log[|\psi_R(t,\mu_0)|]$. (b) A linear fit to the maxima of $\log[|\psi_R(t,\mu_0)|]$. The slope of this line determines γ_R. (c) The solution $\psi_R(t,\mu_0)$, with only the oscillatory part remaining. Performing FFT on it determines γ_I (see Fig. 10). Note that the initial transition time of $1800\tau_H$ was removed from the calculations.

shown in Fig. 3(b). The inner peak of W_I has practically disappeared, and the growth rate is smaller than in Fig. 3(a). In Figs. 4(a) and 4(b) a "nonconstant-ψ" tearing mode is shown. In other words, most of the spatial variation of the perturbed flow W_R is confined to the region of the maximal variations of ψ_R. Viscosity, in Fig. 4(b) adds additional features to the eigenfunctions, slightly reducing the growth rate. The more complex dependence of the solutions on μ is due to the mixing of Kelvin–Helmholtz and tearing instabilities.

The scaling of the growth rates for the inviscid case is presented in Fig. 5. The lower line represents the analytical scaling and has a slope of $-\frac{1}{2}$ on a log–log scale. It fits very well to the calculated points, which were obtained from the type of solutions shown in Fig. 2(a), having values of resistivity $S = 10^3$–10^7, and it agrees with the analytical results in Table I for the constant-ψ case. The lower the resistivity (higher S) the closer the inner peaks of W_R and ψ_I are to the singular surface $\mu = 0$, while W_I and ψ_R remain almost unaffected. This result is expected from the analytic scaling of the inner layer width $\epsilon \sim S^{-2/5}$ [small shear, Fig. 5(b)] and $\epsilon \sim S^{-1/3}$ (high shear). The upper line of Fig. 5(a) has a slope of $-\frac{1}{3}$, in good agreement with the calculated points from the solutions shown in Fig. 4(a) and the nonconstant-ψ tearing mode (Table I). The dashed curve is the imaginary part of γ for the nonconstant-ψ case. The oscillations of the fluid appear to be caused by K–H instability and therefore exhibit a different behavior than γ_R, which is dominated by tearing.

The dependence of the growth rate on the shear param-

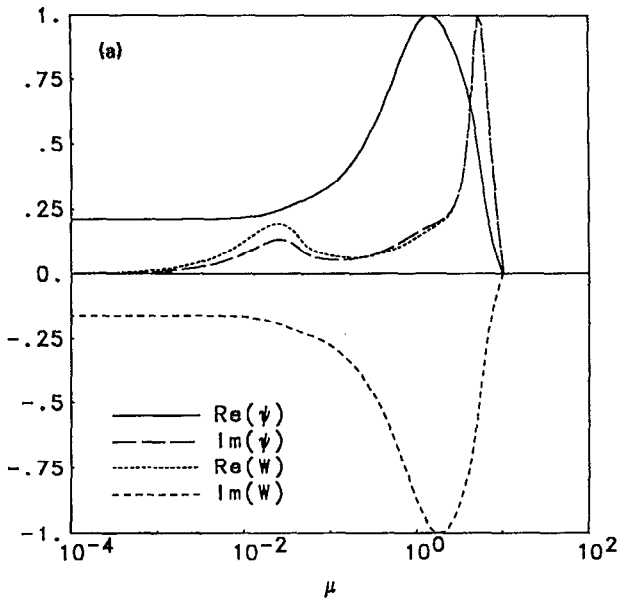

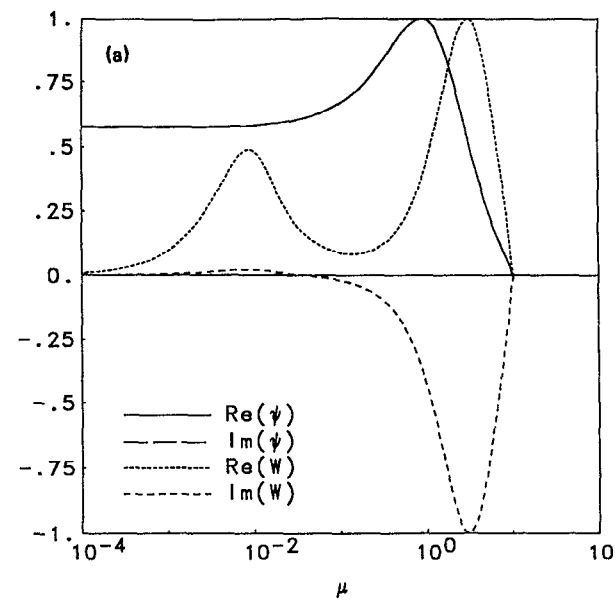

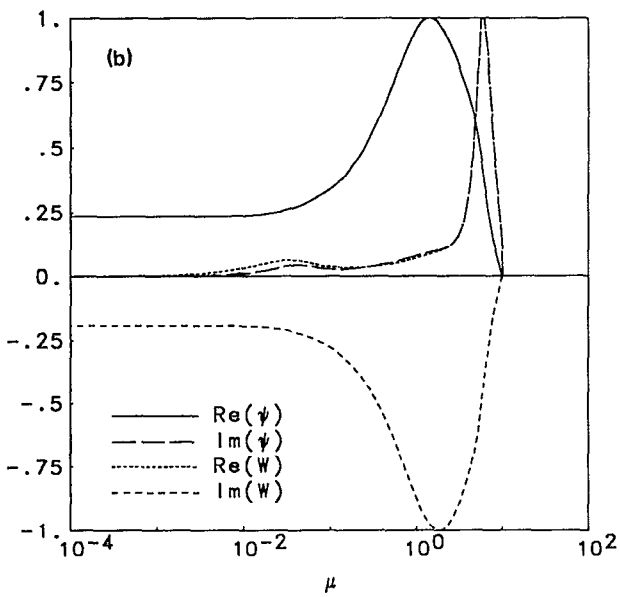

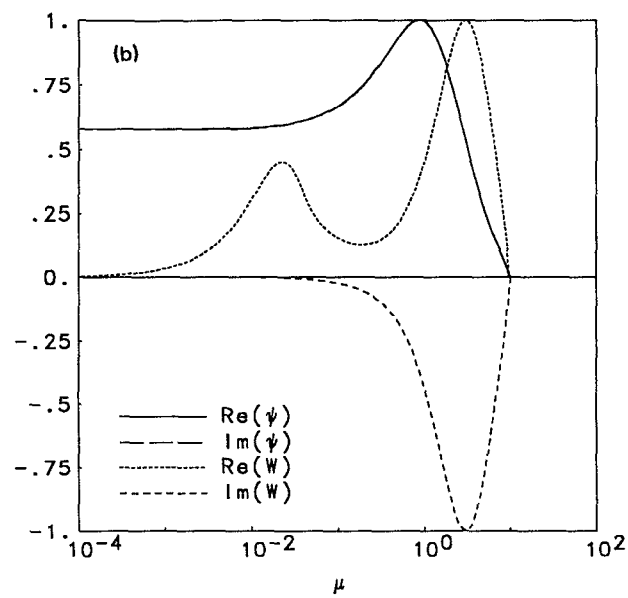

FIG. 2. (a) The spatial variations of the complex solutions W and ψ (inviscid case) normalized to their peak values. The equilibrium flow is $G = V\tanh(R\mu)$, and the parameters are $V = 1$, $R = 0.73$, $S = 10^6$, and $\alpha = 0.5$. (b) Same as (a) except viscosity $S_v = 10^6$.

FIG. 3. (a) Plot of W and ψ as in Fig. 2 except the equilibrium flow is $G = V[\mathrm{sech}(R\mu) - 1]$ and the parameters are $V = 1$, $R = 0.44$, $S = 10^6$, $\alpha = 0.5$, and the notation is the same as in Fig. 2. (b) Same as (a) except viscosity $S_v = 10^6$.

TABLE II. The maximal absolute values of the solutions in Figs. 2–4.

	Fig. 2(a)	Fig. 2(b)	Fig. 3(a)	Fig. 3(b)	Fig. 4(a)	Fig. 4(b)
ψ_R	1.000	1.000	1.000	1.000	1.000	1.000
ψ_I	0.145	0.129	0.218	$0.490\cdot10^{-1}$	1.798	2.156
W_R	0.145	0.129	$0.596\cdot10^{-1}$	$0.135\cdot10^{-1}$	1.851	2.166
W_I	0.897	0.898	0.271	0.271	0.984	1.081

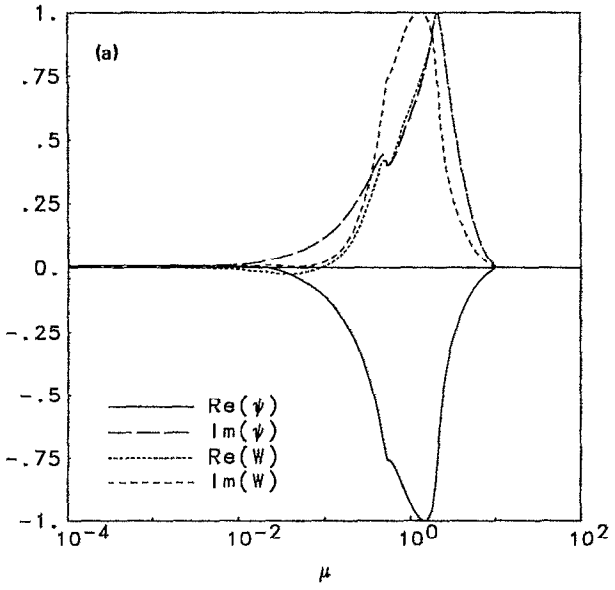

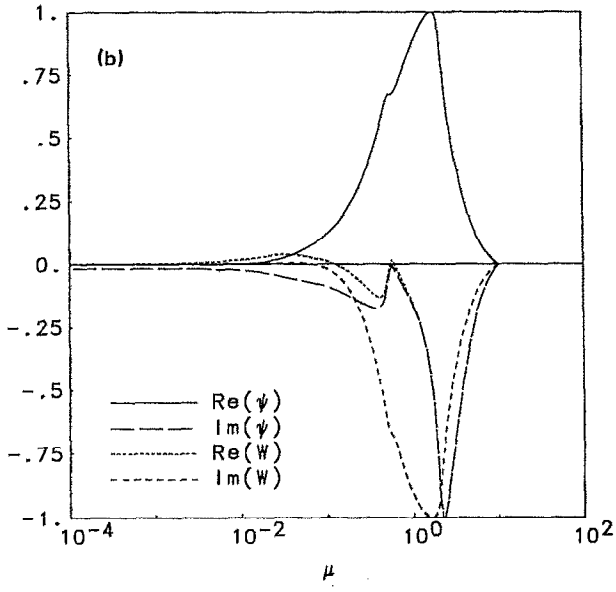

FIG. 4. (a) Same as Fig. 3(a) with $R = 2.5$. (b) Same as Fig. 3(b) with $R = 2.5$.

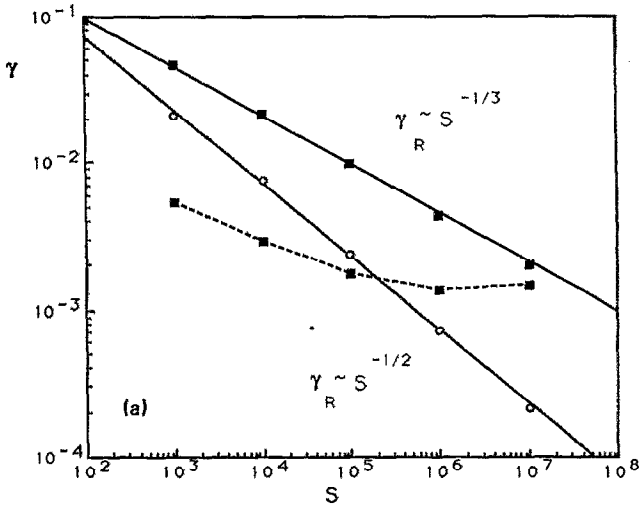

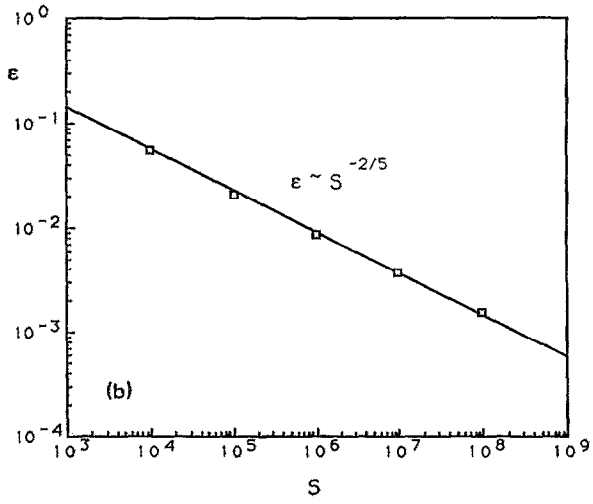

FIG. 5. (a) Growth rate scaling versus S for $V = 1$, $R = 2.5$, $\alpha = 0.5$, and the sech flow profile, the nonconstant-ψ case (the squares are the calculated points). The scaling for $V = 1$, $R = 0.73$, $\alpha = 0.5$, and the tanh flow profile (the circles are the calculated points). (b) The scaling with S of the inner layer width ϵ, as defined by the inner peak of W_R, for the tanh profile with the parameters $V = 0.1$ and $R = 0.5$.

eter R for the tanh flow profile (empty circles) and the sech profile (full circles) is shown in Fig. 6. The real part of the growth rate γ_R agrees with the results, obtained with a different numerical approach, in Ref. 10. For small values of R the FKR growth rate is recovered. When R is of order one ($R = 0.73$), the tanh profile produces a peak in the growth rate, which satisfies conditions (12b)–(12d) and scales as $S^{-1/2}$ (13a). The sech profile produces a different behavior for $R > 1$, namely the solutions become nonconstant-ψ solutions and the tearing mode is further destabilized. The nonconstant-ψ is most evident for $2 < R < 3$ with $V = 1$. At $R > 4$ a transition to ideal K–H instability occurs.[5,10] The oscillating part appears in the nonconstant-ψ regime and reaches its peak value near the transition point to ideal instability.

The matching quantity Δ' was estimated numerically for the solutions in Figs. 2–4 by calculating ψ'/ψ near the singular layer. It was found that Δ' is drastically affected by the flow in the outer region (e.g., by the value of R), while almost unaffected by the resistivity. For the constant-ψ case $\Delta' \sim O(10)$ and for the nonconstant-ψ case $\Delta' \sim O(100)$, in agreement with the analytical calculation of Ref. 5.

When the viscosity is comparable to or larger than resistivity, and with no shear flow, the classical FKR scaling (11) changes to (13d). In Fig. 7 the dependence of the

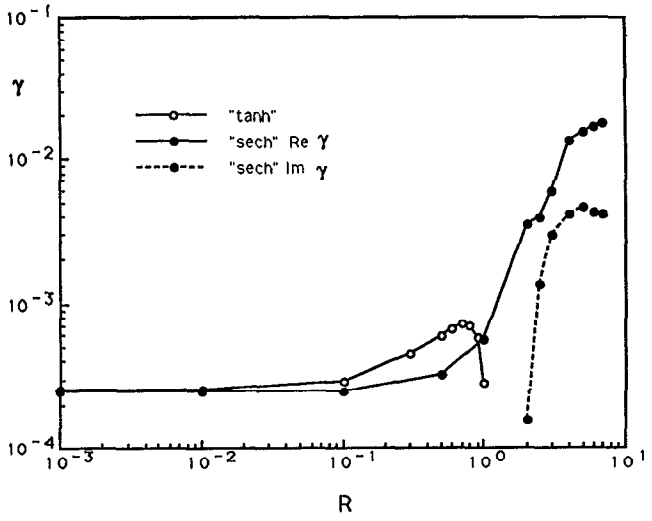

FIG. 6. The growth rate as a function of the shear parameter R, where $S = 10^6$, $V = 1$, $\alpha = 0.5$, for the tanh (empty circles) and sech (full circles) equilibrium flows. The peak is located at $R = 0.73$. For small values of R, the FKR growth rate is recovered.

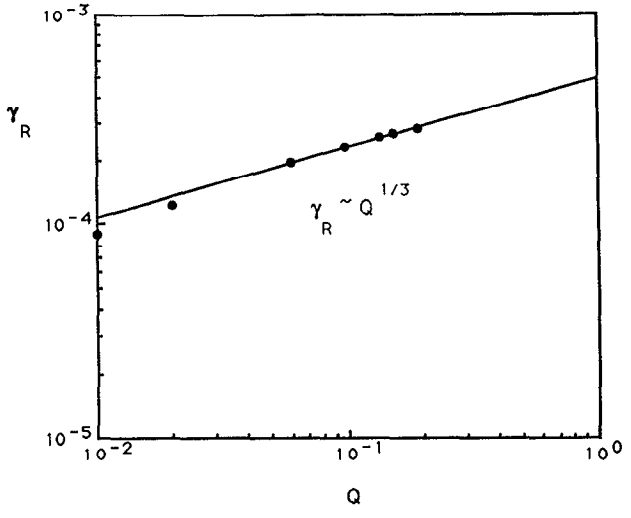

FIG. 8. The dependence of the growth rate on Q [Eq. (13c)] for $S = S_v = 10^6$, $V = 1$, $\alpha = 0.5$. The straight line represents the analytical dependence of $Q^{1/3}$.

growth rate on S_v is shown. The line with the theoretical slope of $\frac{1}{6}$ agrees with the calculated points, which have a least-mean-square slope of 0.168. In Fig. 8 the dependence of the growth rate on Q [Eq. (13c)] is verified and is found to agree well with the analytical result in the range $0.02 < Q < 0.2$. When Q is very small, the influence of flow on the matching quantity Δ' should be accounted for in the analytical growth rate scaling, thereby modifying (13c). (Note that in the numerical solutions ψ and ψ' are continuous everywhere and, therefore, Δ' is not well defined.)

The dependence of the growth rate on viscosity for the sech profile is presented in Fig. 9. For $R = 0.44$, $V = 1$ the analytical scaling of $S_v^{1/6}$ is recovered (lower straight line). For $R = 6$ (high shear) the tearing mode is stabilized, and the instability becomes a Kelvin–Helmholtz mode. The K–H instability is practically unaffected by intermediate to low viscosity ($S_v = 10^4$–10^8), but for higher viscosity, when the viscous time scale is comparable to the instability growth time scale, the mode is stabilized ($S_v < 10^3$) in agreement with the results in Ref. 11. It is interesting to note that the imaginary part of the growth rate exhibits similar behavior to the real part, unlike γ_I in Fig. 6 where both K–H and tearing instabilities are present.

In Fig. 10 an example of the dependence of γ_I on viscosity is shown. For the sech flow profile, $R = 6$ and $S_v = 10^6$ [Fig. 10(a)], only one value for γ_I is found, and it corre-

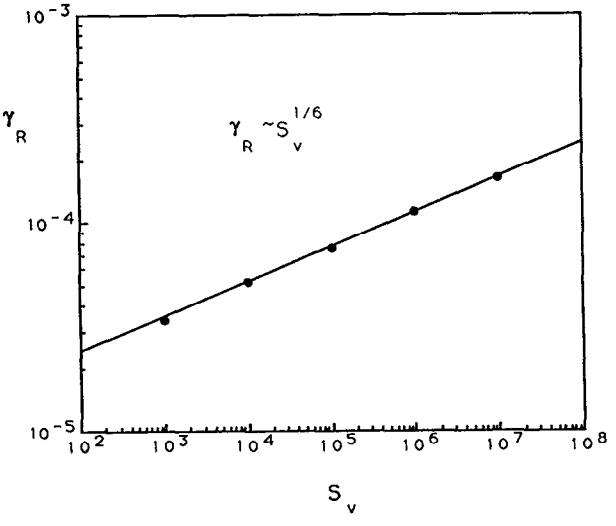

FIG. 7. Calculated numerical growth rate scaling with viscosity parameter S_v. The other parameters are $S = 10^6$, $V = 0$, $\alpha = 0.5$.

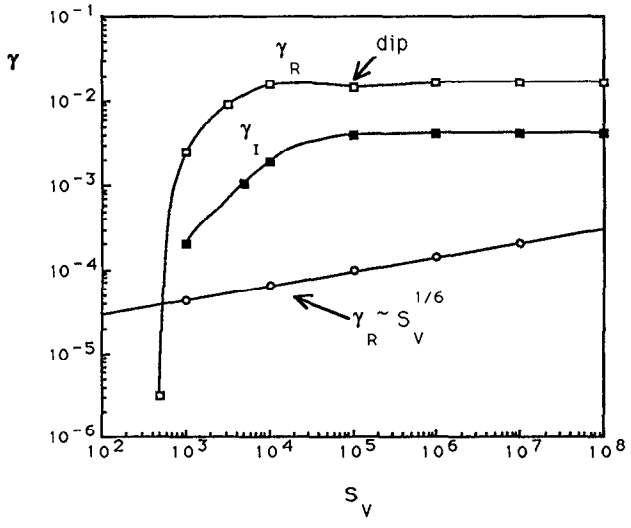

FIG. 9. Dependence of the growth rate on S_v for the sech flow profile and small shear: $V = 1$, $R = 0.44$, and $\alpha = 0.5$. The analytical scaling is recovered (empty circles). For $R = 6$, the transition to ideal Kelvin–Helmholtz instability occurs (the squares are the calculated points).

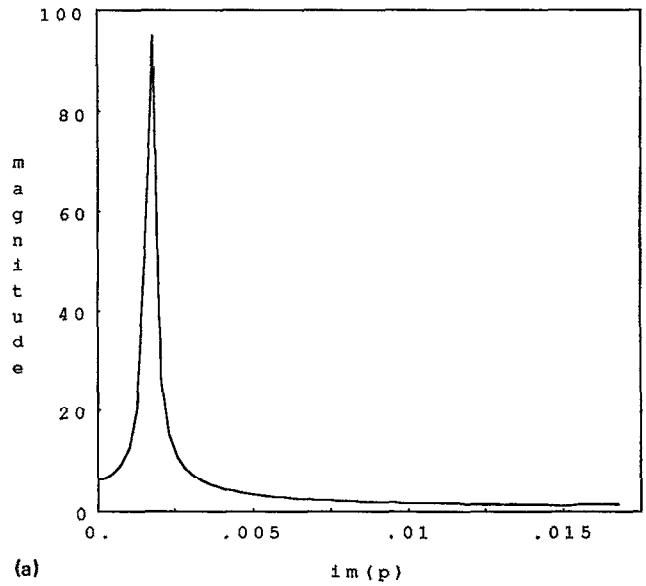

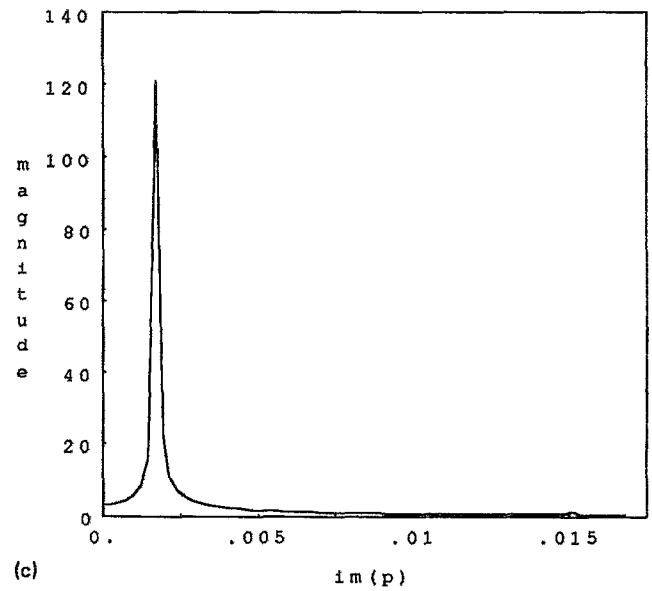

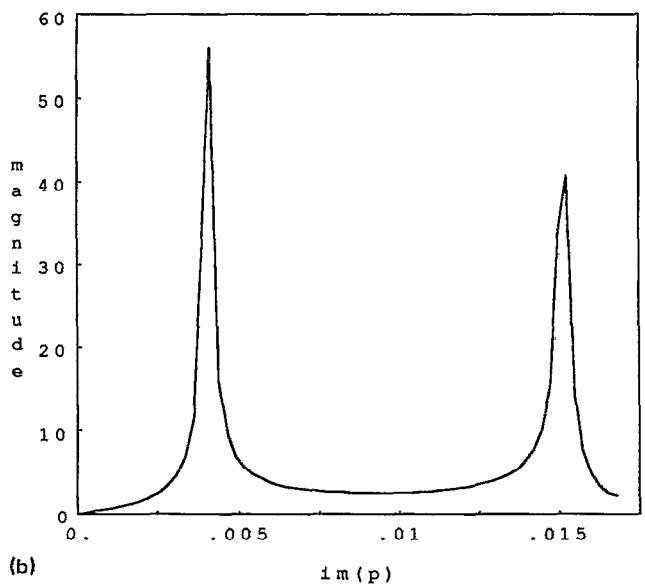

FIG. 10. (a) Determination of γ_I for the sech profile in Eq. (7b) using an FFT for $V=1$, $R=6$, $S=10^6$, $\alpha=0.5$, and (a) $S_v=10^6$, (b) $S_v=10^5$, (c) $S_v=10^4$. Here $\mathrm{Im}(p)$ is the frequency in units of τ_A^{-1} and the locations of the peaks render the values of γ_I.

sponds to the fastest growing mode. When the viscosity is increased and $S_v=10^5$, two overstable modes are present in the solution [Fig. 10(b)] due to condition (18). The growth rate of the fastest growing mode for this value of viscosity has a local minimum (with respect to S_v), and is shown in Fig. 9. When the viscosity is further increased to $S_v=10^4$, the difference between γ_{R1} and γ_{R2} increases, and the magnitude of the second mode in Fig. 10(c) becomes very small compared to the fastest growing mode.

The boundary conditions in the above solutions required exponential decay of the solutions to zero at infinity (8). We have found that using conducting wall boundary conditions at large y ($\mu \geqslant 10$) would not change the results significantly.

VI. SUMMARY AND DISCUSSION

The results of an analytic boundary-layer approach were compared to numerical solutions of the time-dependent, linearized, resistive, and viscous MHD equations (4) and (5) for various values of the parameters α, R, V, S, and S_v. In general, a very good agreement with the analytical growth rate scalings was found. Therefore, the approximations used in analytical theory to find the growth rate scalings are found to hold. The spatial variations of the solutions that were not found analytically for the viscous and inviscid cases with flow have been presented. A nonconstant-ψ tearing mode and its parameter range have been found numerically to be in agreement with the analytical predictions. The

numerical growth rate scalings have been calculated and found to agree with the analytical ones, within the given range of their parameters.

The time-dependent MHD equations (4) and (5) for tearing mode instability were solved numerically, without further approximations, in the region of interest. An implicit variable grid tridiagonal finite difference scheme was used to obtain the numerical solutions, and fast Fourier transform techniques were used to find the imaginary part of the growth rate after the real part, the exponential growth rate γ_R, was found. When the shear flow was very small ($V<0.1$, $R<0.1$) in the inviscid case the classical FKR growth rate and inner layer scalings were recovered. When viscosity is present, the growth rate scaling is changed to $\gamma_R \sim S^{-2/3}(S_v/S)^{1/6}$. For the tanh profile, when the shear flow was large, i.e., $|G'/F'| \sim O(1)$ and $S_v/S = 1$, it has been verified that the growth rate scales as $\gamma_R \sim \{1-[G'(0)/F'(0)]^2\}^{1/3}$. For the "sech" profile, a transition from the constant-ψ to nonconstant-ψ tearing mode was observed to be driven by the flow in the outer region (outside of the tearing layer). In particular for $\alpha = 0.5$, $S = 10^6$, $V = 1$, and $2<R<3$ the nonconstant-ψ tearing mode is obtained, with the analytically predicted growth rate scaling $\gamma_R \sim S^{-1/3}$. In case of the tearing mode, small and intermediate values of viscosity, $S_v = 10^7$–10^3, lower the growth rate. For the sech profile and $R>4$, Kelvin–Helmholtz instability is dominant; it is stabilized for higher values of viscosity ($S_v < 10^3$) when the viscous time scale is comparable to the growth time scale.

The advantage of the time-dependent approach over time-independent methods (such as those used in Refs. 10 and 11) is clearly seen when relatively short time scale simulations are performed, where more than one oscillating mode in the magnetic and velocity perturbations is present. This is particularly important for the generalization of the problem to nonlinear studies.[15]

ACKNOWLEDGMENTS

This work was supported by the U.S. Department of Energy, Contract No. DE-FG05-80ET-53088 and National Science Foundation Contract No. ATM-89-96317.

[1] J. S. Dungey, *Cosmic Electrodynamics* (Cambridge U.P., New York, 1958), pp. 98–102.
[2] H. P. Furth, J. Killeen, and M. N. Rosenbluth, Phys. Fluids **6**, 459 (1963).
[3] J. Killeen, in *Physics of Hot Plasmas*, edited by B. J. Rye and J. C. Taylor (Plenum, New York, 1970), p. 212.
[4] R. S. Steinolfson and G. Van Hoven, Phys. Fluids **26**, 117 (1983).
[5] X. L. Chen and P. J. Morrison, Phys. Fluids B **2**, 495 (1990).
[6] X. L. Chen and P. J. Morrison, Phys. Fluids B **2**, 2575 (1990).
[7] F. Porcelli, Phys. Fluids **30**, 1734 (1987).
[8] R. B. Paris and W. N.-C. Sy, Phys. Fluids **26**, 2966 (1983).
[9] M. Dobrowolny, P. Veltri, and A. Mangeney, J. Plasma Phys. **29**, 303 (1983).
[10] G. Einaudi and F. Rubini, Phys. Fluids **29**, 2563 (1986).
[11] G. Einaudi and F. Rubini, Phys. Fluids B **1**, 2224 (1989).
[12] S. Wang, L. C. Lee, and C. Q. Wei, Phys. Fluids **31**, 1544 (1988).
[13] E. R. Priest, *Solar Magnetohydrodynamics* (Reidel, Dordrecht, The Netherlands, 1985); J. Drake, in *IAU Symposium 107*, edited by M. R. Kundu and G. D. Holman (Reidel, Dordrecht, The Netherlands, 1985), p. 61.
[14] S. I. Akasofu, *Physics of Magnetospheric Substorms* (Reidel, Dordrecht, The Netherlands, 1977).
[15] R. S. Steinolfson and G. Van Hoven, Phys. Fluids **27**, 1207 (1984).
[16] J. F. Drake and Y. C. Lee, Phys. Fluids **20**, 134 (1977).
[17] S. I. Braginskii, Rev. Plasma Phys. **1**, 205 (1965).